GreenShield Port Architecture for Multi-Carrier Resiliency Integrating Offshore Wind, Hydrogen Ferry, and Mobile Fuel-Cell Generators

Aligul Selim Turkoglu
SYSTEC-ARISE, FEUP, UPorto
Porto, Portugal
asturkoglu@fe.up.pt

Artur Costa e Sá
FEUP, UPorto
Porto, Portugal
up202006800@edu.fe.up.pt

Sérgio F. Santos
C-MAST, UBI
Covilha, Portugal
sfs@ubi.pt

Ozan Erdinc
SYSTEC-ARISE,
Porto, Portugal
YTU, İstanbul, Türkiye
ozanerdinc@gmail.com

João P. S. Catalão
SYSTEC-ARISE, FEUP, UPorto
Porto, Portugal
catalao@fe.up.pt

***Abstract*—When a coastal feeder island is affected by a disaster, the port is often the only node that can land energy, fuel, and logistics at scale, while offshore resources are less exposed to land-side damage and access constraints. Existing disaster-recovery methods treat generation and logistics in isolation. To this end, this study aims to maximize the restoration of both critical and non-critical loads during prolonged feeder outages while ensuring voltage remains within statutory bounds by introducing the GreenShield Port. This resilience architecture co-optimizes an offshore wind plant with an electrolyzer, a hydrogen ferry, and a fleet of mobile fuel-cell generators (MFGs). A mixed-integer quadratically constrained formulation schedules 15-minute power dispatch and MFG routing/charging on a modified IEEE 33-bus network with the point of common coupling outaged and three critical buses. The main contribution is co-optimizing electricity, hydrogen, and vehicle routing decisions by jointly treating offshore wind, ship-to-grid, and MFGs within a unified resilience framework. In the integrated configuration, coordinated ferry, wind, and MFG resources fully restore critical demand and serve nearly 90% of total energy while maintaining voltages within ±5 %. The integrated port thus co-ordinates ship-to-grid, wind-to-hydrogen, and mobile generation to accelerate service restoration during prolonged outages materially.**

Keywords—Disaster recovery, multi-carrier energy systems, offshore wind power, power system resilience, ship-to-grid.

I. Introduction

The continuity and quality of electrical energy are crucial for sustaining daily life [1]. Disasters increasingly disrupt energy systems, making preparedness for resilience and rapid restoration essential [2]; in particular, integrated coordination of power and gas infrastructures can strengthen disaster-time response. With the frequency and intensity of natural hazards rising under climate change, the vulnerability of energy systems has grown worldwide [3].

Modern grids face widespread outages during hurricanes and cascading failures triggered by wildfires and floods. These pressures underline the need to plan for resilience, the capacity of energy systems to anticipate, absorb, adapt to, and recover from adverse events. Recent resilience studies quantify recovery as the time-integrated unsupplied energy and present the search for functionally critical components as a multi-objective problem, showing that structural and functional criticalities can diverge, thereby sharpening targets for hardening and restoration [4].

In this context, hydrogen—as a storable, dispatchable energy carrier—along with mobility-enabled resources (electric vehicles and ship-to-grid services) provides flexible, localized restoration to prioritized loads during outages, strengthening disaster recovery and operational continuity [5]. Resilience against extreme disruptions is now a central objective for modern power systems. The literature spans pre-event reconfiguration and post-event restoration using distributed energy resources (DERs), mobility, and multi-energy coupling, underscoring the need for integrated restoration frameworks.

On the preventive side, [6] formulates a multi-objective scheduling problem for the IEEE 123-bus system that leverages demand response (DR) to reduce operating costs and improve reliability before potential islanding. Complementarily, [7] builds coastal networked microgrids with marine energy and storage; by sectionalizing critical loads in real time, it sustains continuity under severe weather. Collectively, these works reinforce and reconfigure networks pre-event via DR, distributed generation (DG) placement, sectionalization, and resource diversification.

Following the preventive stream, the post-event literature pivots to fast restoration. For this phase, [8] proposes a two-stage robust optimization that co-ordinates mobile emergency generators, DERs, and DR to reduce load loss and investment while accelerating recovery. Within this phase, a complementary line integrates Q-learning–based sequential repair with fast, optimal power dispatch on the evolving topology, maximizing delivered energy along the restoration staircase at a fraction of the exhaustive-search cost [9]. Mobility-centric works dispatch truck generators in staged sequences to re-energize prioritized loads [10]. At the same time, [11] co-optimizes EV routing and scheduling across power and heat to flexibly restore local demand. Beyond electricity-only strategies, interdependent power–hydrogen operation [12] couples local generation with stored H_2 to serve critical electricity, heat, and hydrogen needs during outages, further shortening recovery times.

Existing studies address mobile fuel-cell generators (MFGs), vessel-to-grid support, and offshore power-to-hydrogen schemes in isolation. However, significant gaps persist regarding the coordinated use of MFGs, hydrogen ferries, and offshore wind-electrolyzer hybrids to create a unified, port-centered resilience solution.

979-8-3315-8138-1

To bridge this gap, a GreenShield Port architecture is proposed that embeds all assets within a single framework. The **novel contributions** are fourfold:

- GreenShield Port is introduced as a port-centric resilience hub that provides a replicable template for disaster-resilient maritime energy infrastructure.
- A dual-mode ferry model is developed that schedules onboard fuel-cell output while simultaneously acting as the sole hydrogen depot for mobile generators.
- A depot-aware routing formulation dispatches fuel-cell mobile generators from the ferry, accounting for hydrogen inventory and travel times to minimize restoration delays.
- An offshore wind turbine with an integrated electrolyzer operates as both a generator and a green-hydrogen source, ensuring a continuous fuel supply when onshore infrastructure is compromised.

II. Methodology

In this framework, multiple medium-voltage buses within the distribution network accommodate critical loads which must be fulfilled under disaster conditions. When a disruptive event occurs in any segment of the grid, MFGs—administered by a dedicated fleet operator—are dispatched as ancillary power resources to supply those prioritized loads. To avert extensive load shedding, MFGs travel from a designated seaport refueling hub to the critical nodes to accelerate restoration. Additionally, the hydrogen ferry operator can provide ancillary power via onboard fuel cells. This coordinated strategy—fostered by two-way information exchange between the fleet operator and the ferry operator—enables an optimal recovery solution that upholds reliable service in disaster scenarios. The proposed energy supply mechanism is depicted in Fig. 1.

Eq. (1) maximizes the total supplied power over the scheduling horizon. The first term sums the grid-served portion of demand across all nodes and time steps after per-unit normalization with $\boldsymbol{S_{base}}$; the second term adds the mobile fleet's contribution at the critical nodes. Together, these terms drive the optimiser to allocate ferry, wind, and MFG resources so that the critical load is restored. At the same time, any available surplus is pushed to the grid.

$$O.F. = max\{\sum_{t\in\mathcal{T}}\sum_{i\in\mathcal{N}} S_{base}\ P_{i,t}^{fulfilled\_from\_grid} + \sum_{t\in\mathcal{T}}\sum_{i\in\mathcal{N}^d} P_{i,t}^{fulfilled\_from\_MFGs}\} \quad (1)$$

Eqs (2)–(3) enforce Kirchhoff-style active and reactive power balance at the slack substation in each period. The left-hand sides collect the ferry's injection $\boldsymbol{P_{i,t}^{\text{ship\_to\_grid}}}$, $\boldsymbol{Q_{i,t}^{\text{ship\_to\_grid}}}$, wind injection to the grid $\boldsymbol{P_{t}^{\text{Wind\_to\_grid}}}$ and the net flow terms, while the right-hand sides match total network losses plus the demand portion served directly by the grid $\boldsymbol{P_{i,t}^{\text{fulfilled\_from\_grid}}}$, $\boldsymbol{Q_{i,t}^{\text{demand}}}$.

Line losses are represented by (4)–(5). For each branch $\boldsymbol{i,j}$, the active (resp. reactive) loss equals the branch resistance $\boldsymbol{R_{i,j}}$ (resp. reactance $\boldsymbol{X_{i,j}}$) times the squared magnitude of active and reactive flow components, scaled by $\boldsymbol{V_0^2}$, which is the squared slack-bus voltage. This quadratic form preserves the impact of both active and reactive flows on losses.

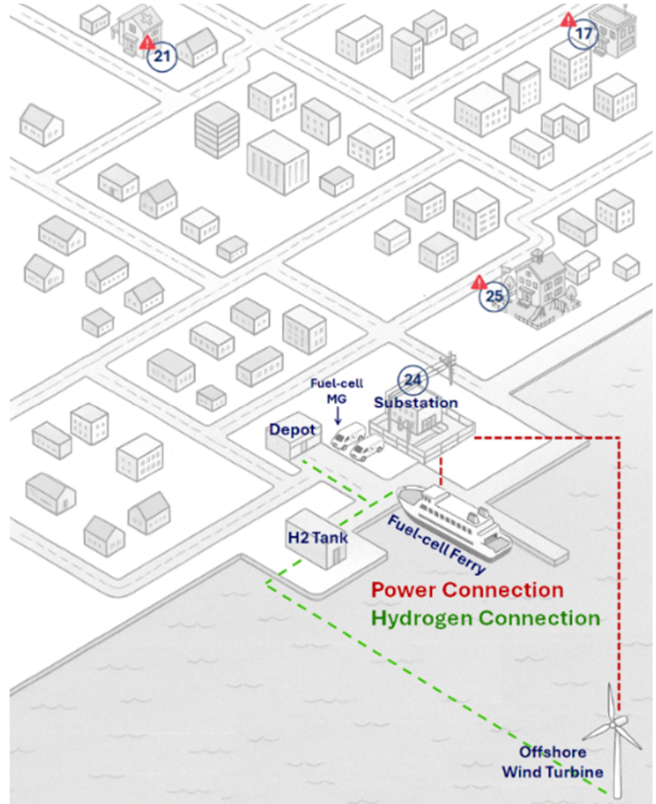

Fig. 1. A general scheme for the proposed energy supply mechanism

Voltage behavior along a feeder is captured by (6), where the downstream voltage equals the upstream voltage minus the drop caused by branch impedance and power flow, normalized by $\boldsymbol{V_0}$. Limits in (7) keep all non-slack node voltages inside [$\boldsymbol{V_i^{min}}$, $\boldsymbol{V_i^{max}}$], ensuring service quality during restorations.

$$P_{i,t}^{ship\_to\_grid} + P_{t}^{Wind\_to\_grid} + \sum_{j\in\Omega_i^o} P_{i,j,t}^{f} - \sum_{j\in\Omega_i^i} P_{j,i,t}^{f} = \sum_{j\in\Omega_i} P_{i,j,t}^{loss} + P_{i,t}^{fulfilled\_from\_grid} \quad (2)$$

$$Q_{i,t}^{ship\_to\_grid} + \sum_{j\in\Omega_i^o} Q_{i,j,t}^{f} - \sum_{j\in\Omega_i^i} Q_{j,i,t}^{f} = \sum_{j\in\Omega_i} Q_{i,j,t}^{loss} + Q_{i,t}^{demand} \quad (3)$$

$$P_{i,j,t}^{loss} = R_{i,j}\ \left(P_{i,j,t}^{f}\right)^2 + \left(Q_{i,j,t}^{f}\right)^2 / V_0^2 \quad (4)$$

$$Q_{i,j,t}^{loss} = X_{i,j}\ \left(P_{i,j,t}^{f}\right)^2 + \left(Q_{i,j,t}^{f}\right)^2 / V_0^2 \quad (5)$$

$$V_{j,t} = V_{i,t} - (R_{i,j}\, P_{i,j,t}^{f} + X_{i,j}\, Q_{i,j,t}^{f})/V_0 \quad (6)$$

$$V_i^{min} \le V_{i,t} \le V_i^{max} \quad (7)$$

Eq. (8) partitions the offshore wind turbine output between direct grid injection and hydrogen production. The variable $\boldsymbol{P_{t}^{\text{Wind\_to\_grid}}}$ translates to real-power injection after multiplying by $\boldsymbol{S}_{\text{base}}$, while the residual $\boldsymbol{P_{t}^{\text{Wind\_to\_tank}}}$ is converted to hydrogen for storage.

$$P_{t}^{Wind\_Gen} = P_{t}^{Wind\_to\_grid} \cdot S_{base} + P_{t}^{Wind\_to\_tank} \quad (8)$$

The tank inventory at the GreenShield Port follows the mass balance (9): the new level equals the previous level plus wind-produced hydrogen, minus the hydrogen dispensed to MFGs for refueling and minus the hydrogen consumed by the ferry's fuel cells when generating power for the grid. Initialization is given by (10). Eq. set (11) links power quantities to hydrogen mass through the conversion coefficient α (kWh per kg). It converts wind-to-tank power, tank-to-MFGs refueling power, and ship-to-grid power into their hydrogen equivalents, ensuring the electrical and fuel subsystems remain consistent.

979-8-3315-8138-1

Table I. Travelling Time

From	To	Travelling Time (nº time periods - minutes)
17	21	3 – 45m
17	24	4 – 60m
17	25	5 – 75m
21	24	5 – 75m
21	25	4 – 60m
24	25	3 – 45m

Table II. Considered Cases Summary

Case	H_2 Ferry → MFGs	H_2 Ferry → Grid	Offshore Wind Turbine	Hydrogen Tank
1	yes	no	no	no
2	yes	yes	no	no
3	yes	yes	yes	yes

Table III. Node-Level Support Profile (Case 3)

Node	Avg. MFG Output (kW)	Max (kW)	Time of Peak	Duty Factor (%)	Grid Supplement (kWh)	Voltage Min (p.u.)
17	40.81	158.12	9:00	44.79%	775.92	0.987
21	10.12	36.49	17:45	38.54%	247.57	1.019
25	27.21	87.61	14:45	44.79%	521.79	1.007

Table IV. Fleet Mission Chronicle (Case 3)

Vehicle	First Departure	Last Return	Relocations	Vehicle hours (h)	Energy Delivered (kWh)	Avg. Discharge rate (kW)	Stops at nodes (17/21/25/24)
1	3:00	—	6	8.25	391.20	53.96	(3/3/0/1)
2	3:00	—	4	7.50	500.00	68.97	(2/0/2/1)
3	7:15	15:15	5	9.25	304.39	41.98	(2/2/0/2)
4	3:00	15:45	6	5.75	269.60	53.92	(1/2/2/2)
5	3:00	21:45	6	8.50	150.98	50.33	(2/0/2/3)
6	3:00	15:30	4	7.75	259.19	51.84	(0/1/2/2)

$$Tank_t^{Level} = Tank_{t-1}^{Level} + m_t^{Wind\_to\_tank} - m_{i,t}^{Tank\_to\_MFGs} - m_{i,t}^{ship\_to\_grid} \qquad \forall t > 0,\ i = 24 \tag{9}$$

$$Tank_0^{Level} = Tank^{Init} \tag{10}$$

$$m_t^{Wind\_to\_tank} = P_t^{Wind\_to\_tank}\alpha, \quad m_{i,t}^{Tank\_to\_MFGs} = P_{i,t}^{Tank\_to\_MFGs}\alpha, \quad m_{i,t}^{ship\_to\_grid} = P_{i,t}^{ship\_to\_grid}\alpha \tag{11}$$

At each service node $\boldsymbol{i}$, (12) enforces energy balance between the tank and the local MFG activity. If the node hosts the depot $\boldsymbol{u}_{\boldsymbol{i}}^{\text{Depot}}$=1, total MFG charging power plus any local supply must be supported by the tank-to-MFGs flow; otherwise, the MFG discharge equals the local MFG-served demand.

Eq. (13) couples total fleet charging power at a node to the hydrogen mass drawn from the tank via $\boldsymbol{\alpha}$. Constraints (14)–(15) limit served demand: non-critical nodes can only be supplied by the grid, while critical nodes may be split between the grid and the MFGs, but cannot exceed their native demand after $\boldsymbol{S}_{\text{base}}$ denormalization.

The big-M constraints (16)–(17) restrict refueling to the depot by forcing tank-to-MFGs power and the associated hydrogen mass to zero whenever $\boldsymbol{u}_{\boldsymbol{i}}^{\text{Depot}}$=0. Finally, (18) tightens the local balance at non-depot nodes by equating the MFG discharge at those nodes to the MFG-served demand.

$$P_{i,t}^{MFG\_ch\_tot}\, u_i^{Depot} + P_{i,t}^{fulfilled\_from\_MFGs} = P_{i,t}^{Tank\_to\_MFGs}\, u_i^{Depot} + P_{i,t}^{MFG\_disch\_tot} \tag{12}$$

$$m_{i,t}^{MFG\_ch\_tot} = P_{i,t}^{MFG\_ch\_tot} \tag{13}$$

$$P_{i,t}^{fulfilled\_from\_grid} \le P_{i,t}^{demand} \qquad i \notin \mathcal{N}^d \tag{14}$$

$$S_{base}\, P_{i,t}^{fulfilled\_from\_grid} + P_{i,t}^{fulfilled\_from\_MFGs} \le P_{i,t}^{demand} \qquad i \in \mathcal{N}^d \tag{15}$$

$$P_{i,t}^{Tank\_to\_MFGs} \le M\, u_i^{Depot} \tag{16}$$

$$m_{i,t}^{MFG\_ch\_tot} \le M\, u_i^{Depot} \tag{17}$$

$$P_{i,t}^{MFG\_disch\_tot} = P_{i,t}^{fulfilled\_from\_MFGs} \tag{18}$$

Eqs. (19)–(20) define, at each node and time, the total hydrogen mass charged and the total electric power discharged by the fleet, each computed as the sum over vehicles. Constraints (21)–(22) impose vehicle-level operating limits and prevent simultaneous charge and discharge through a binary charge/discharge indicator. Presence constraints (23)–(24) ensure physical feasibility: a vehicle may only discharge or refuel if it is actually at the node $\boldsymbol{u}_{\boldsymbol{i,t,f}}^{\text{MFG}}$=1. Together, (19)–(24) provide bounds on per-vehicle and per-site operations.

$$m_{i,t}^{MFG\_ch\_tot} = \sum_{f \in y} m_{i,t,f}^{MFG\_ch} \tag{19}$$

$$P_{i,t}^{MFG\_disch\_tot} = \sum_{f \in y} P_{i,t,f}^{MFG\_disch} \tag{20}$$

$$m_{i,t,f}^{MFG\_ch} \le I_m^{MFG}(1 - u_{i,t,f}^{CD}) \tag{21}$$

$$P_{i,t,f}^{MFG\_disch} \le I_P^{MFG}\, u_{i,t,f}^{CD} \tag{22}$$

$$P_{i,t,f}^{MFG\_disch} \le I_P^{MFG}\, u_{i,t,f}^{MFG} \tag{23}$$

$$m_{i,t,f}^{MFG\_ch} \le I_m^{MFG}\, u_{i,t,f}^{MFG} \tag{24}$$

For each vehicle $\boldsymbol{f}$, the hydrogen state evolves according to (25): the State of Energy (SoE) at time $\boldsymbol{t}$ equals the previous SoE plus the integrated refueling flow minus the integrated discharge across all nodes, scaled by the time step $\boldsymbol{\Delta T}$. Eq. (26) sets the initial SoE, and Eq. (27) bounds the SoE within the safe operating window for the onboard tank.

$$m_{f,t}^{MFG} = m_{f,t-1}^{MFG} + \Delta T \sum_{i \in \mathcal{N}} m_{i,t,f}^{MFG\_ch} - \Delta T \sum_{i \in \mathcal{N}} m_{i,t,f}^{MFG\_disch} \tag{25}$$

$$m_{f,0}^{MFG} = m_{init}^{MFG} \tag{26}$$

$$m_{min}^{MFG} \le SoE_{f,t}^{MFG} \le m_{max}^{MFG} \tag{27}$$

Constraint (28) enforces minimum travel time between distinct service points by disallowing a new arrival within $\boldsymbol{T}_{\boldsymbol{i,j}}^{\text{Travel}}$ periods after a departure. Eq. (29) updates the presence variable: the difference between arrivals and departures matches the change in presence at the node. Constraint (30) forbids arriving and departing in the same period. Finally, (31) initializes the fleet: every MFG starts the horizon at the depot node $\boldsymbol{i = 24}$.

$$\sum_{l=t-T_{i,j}^{Travel}+1}^{t} z_{i,l,f}^{MFG} \le 1 - y_{i,f,t}^{MFG} \qquad for\ \ t - T_{i,j}^{Travel} + 1 > 0 \tag{28}$$

$$y_{i,f,t}^{\text{MFG}} - z_{i,f,t}^{\text{MFG}} = u_{i,f,t}^{\text{MFG}} - u_{i,f,t-1}^{\text{MFG}} \tag{29}$$

$$y_{i,f,t}^{\text{MFG}} + z_{i,f,t}^{\text{MFG}} \le 1 \tag{30}$$

III. Case Studies and Analysis

The proposed optimization framework is implemented in GurobiPy as a mixed-integer quadratically constrained program and simulated on a modified IEEE 33-bus distribution network over a 24-hour horizon with 15-minute intervals. As shown in Fig. 2, the system is islanded by an outage at Node 0, while the GreenShield Port is interfaced at Node 24, which serves as the slack bus with voltage fixed at its nominal level; per-unit bases follow the IEEE test network ($V_{base} = 12.66\ kV$). Moreover, ratings are scaled to a 1 MW nominal power level. Three critical buses (17, 21, 25) act as discharging points for a fleet of MFGs, whose capacities are each sized at 10 kg H_2, initialized empty, and subject to per-interval limits of 25 kWh discharge and 10 kg refueling; vehicle travel times are given in Table I, and travel costs are neglected.

979-8-3315-8138-1

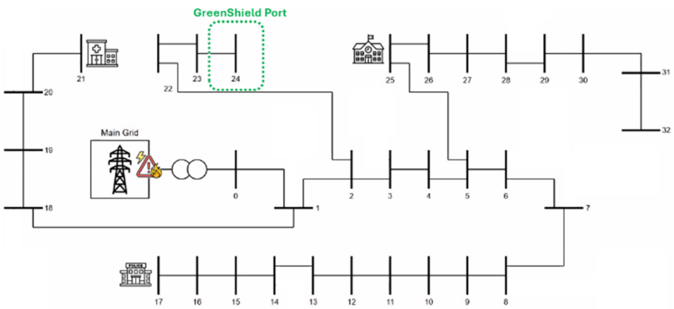

Fig. 2. IEEE 33-Bus Distribution Test Network

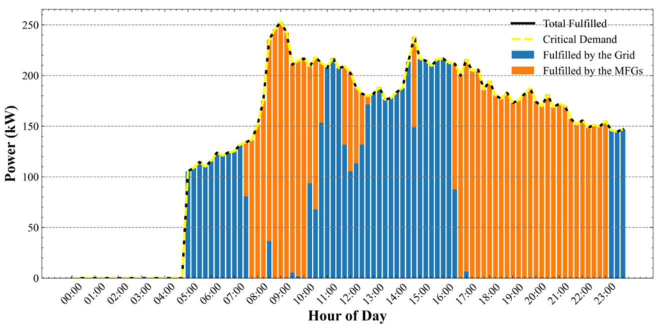

Fig. 3. Total Fulfilled Power vs. Aggregate Critical Node Demand (Case 3)

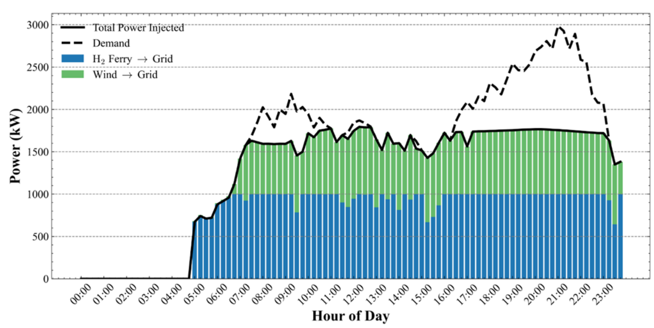

Fig. 4. Total Injection vs. Aggregate Grid Demand (Case 3)

Critical-node demand time series were sourced from a public industrial/commercial dataset collected under extreme-weather conditions [13]. In contrast, the remaining bus demands follow the canonical IEEE 33-bus benchmark profiles. The GreenShield Port comprises a single depot for MFG refueling, a hydrogen ferry equipped with onboard fuel cells that can provide auxiliary power, an offshore wind plant dispatched either directly to the grid or to electrolysis, and a pressurized hydrogen tank rated at 800 kg. The wind profile is derived from a Vestas V90-2000 at 80 m hub height, but it is operated at a 1 MW installed capacity. Voltage limits are enforced at ±5% around nominal on all buses.

This study evaluates the GreenShield concept across three case families (Cases 1–3), each comprising 6 MFGs. Case 1 represents the baseline: MFGs alone supply selected critical nodes while the hydrogen ferry only refuels them. Case 2 extends the setup by allowing the ferry to inject power into the islanded grid via onboard fuel cells, in addition to refueling. Case 3 adds an offshore wind turbine and electrolyzer; wind supplies the grid and produces hydrogen, while storage capacity is explicitly modelled. The configuration matrix for all cases is provided in Table II.

Fig. 3 compares the total power supplied by the MFG fleet and the grid with the aggregate critical-load demand for Case 3. The two traces align closely, indicating adequate demand coverage. The grid's role is concentrated in three windows: an early-morning surge from 05:00–07:30 h where it delivers ≈114.7 kW on average; a midday interval from 10:15–16:30 h when grid power ramps up as MFG output tapers; and a late-night bump around 23:15 h after a period of zero contribution. During 16:45–23:00 h, the MFGs shoulder most of the service at ≈175.5 kW average. Daily totals split to 1.54 MWh from the grid (45.2%) and 1.87 MWh from the MFGs (54.8%).

Fig. 4 shows the grid demand with injections from the hydrogen ferry and offshore wind turbine. From 05:00–06:45 h, the ferry ramps to cover the early spike; once the turbine comes online, the combined output reaches ≈1.5 MW. Throughout the day, the ferry holds near 1.0 MW, while wind varies between 0.6 and 0.8 MW, yielding a combined average near 1.7 MW. Even so, morning and evening peaks exceed this supply, producing a maximum shortfall of ≈1.18 MW at the demand crest.

During the day, the hydrogen ferry contributes 18.1 MWh—about 50.8% of total demand—while the offshore wind turbine adds 12.8 MWh (35.8%). Together, they inject 30.9 MWh, covering roughly 84% of the system's energy needs.

Viewed with Figs. 3–4, this positions the MFG fleet as a flexible reliability reserve: when the combined ferry-plus-wind output falls short, the optimization redirects MFGs to priority nodes to serve critical loads, leaving the ferry and turbine to supply non-critical demand. The effect is most evident during demand peaks, where the fleet closes the gap and preserves uninterrupted service despite a system-wide generation deficit.

Table III indicates that Node 17 receives the largest share of mobile-generation support—979.37 kWh, or 52% of fleet output—followed by Node 25 with 653.10 kWh (34%) and Node 21 with 242.90 kWh (13%). Nodes 17 and 25 exhibit identical duty factors of 44.79%, showing that MFGs serve these buses for nearly half of the day.

Table V. Daily Energy Ledger

Case	Critical Load served by MFGs [MWh]	Critical Load served by Grid [MWh]	Total Critical Load served [MWh]	Tank Discharge → Fleet [MWh]	Tank Discharge → Grid [MWh]	Tank Discharge (Fleet + Ferry) [MWh]	Wind → Tank [MWh]	Wind → Grid [MWh]	Total Load Served [MWh]
1	3.38 (98.73%)	–	3.38 (100%)	3.38 (100%)	–	3.38 (100%)	–	–	3.38 (9.47%)
2	3.221 (94.2%)	0.200 (5.8%)	3.42 (100%)	3.221 (14.71%)	18.673 (85.29%)	21.893 (100%)	–	–	21.51 (60.34%)
3	1.875 (54.8%)	1.545 (45.2%)	3.42 (100%)	1.875 (9.33%)	18.223 (90.66%)	20.098 (100%)	5.082 (28.46%)	12.775 (19.89%)	31.83 (89.26%)

979-8-3315-8138-1

In contrast, Node 21's lower duty factor (38.54%) and higher grid supplement (247.57 kWh) signal greater reliance on grid supply. Average/peak MFG outputs are 40.81/158.12 kW at Node 17, 10.12/36.49 kW at Node 21, and 27.21/87.61 kW at Node 25, with peaks at 09:00, 17:45, and 14:45, respectively. The minimum voltage remains within the limits (0.987–1.019 p.u.), confirming adequate voltage support. At the same time, the fleet focuses on the two higher-demand nodes.

Table IV highlights a leaner fleet in Case 3. Vehicle 2 leads with 500 kWh delivered at an average 68.97 kW over 7.5 h, while Vehicle 1 follows with 391.20 kWh at 53.96 kW over 8.25 h. The remaining units operate at ≈42–53.9 kW, delivering 150.98–304.39 kWh each. Across the day, the model schedules 31 relocations (≈5 per vehicle) for 47 vehicle-hours out of 120 available, resulting in about 39.17% fleet utilization and a combined output fluctuating between 150 and 300 kW.

Fig. 5 shows the average voltage profile of the nodes in Case 3. The GreenShield Port at Node 24 serves as the slack and primary injection point (ferry + offshore wind), keeping the backbone near 1.05 p.u. and supporting the most significant local demand at Node 23. The average voltage map highlights the expected radial gradients: the 6h-17h spur exhibits the steepest drop, making Node 17 the bottleneck; its daily average is ≈1.02–1.03 p.u., consistent with the recorded minimum of 0.987 p.u. The 25–32 lateral shows moderate sag, with Node 25 averaging around ≈1.03 p.u. (minimum 1.007 p.u.), while the west lateral ending at Node 21 remains comparatively stronger, averaging ≈1.03–1.04 p.u. (minimum 1.019 p.u.).

System-wide, the Case-3 mean voltage hovers near 1.03–1.04 p.u. and briefly dips during the evening peak yet stays within the ±5% limit. Targeted MFG dispatch to Nodes 17 and 25 during high-load windows helps flatten local drops. In contrast, continuous injection at Node 24 preserves headroom along the main corridor.

Across the three scenarios, capability steps up from MFG-only to ferry-assisted and finally to a multi-energy port as seen in Table V. In Case 1, six MFGs cover 98.7% of the critical load, demonstrating that optimized routing/charging nearly eliminates unmet demand while serving only the essential subset of the network. Moving to Case 2, ferry injection closes the remaining gaps, restores 100% of the critical demand, and the system serves 60.3% of total daily demand, with the ferry delivering 18.67 MWh (≈52.3%) of the overall load.

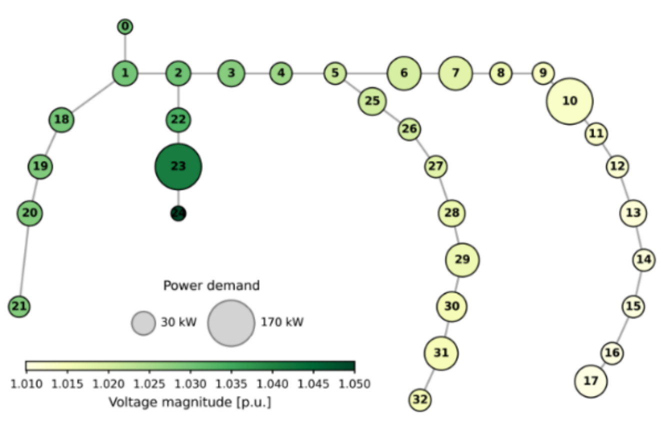

Fig. 5. Average Voltage Profile of the Nodes (Case 3)

In Case 3, integrating offshore wind and a finite tank shifts MFGs into a reserve role: the MFG share of critical supply falls to 54.8–52.9%, while wind adds ≈12.78 MWh directly to the grid and total load served jumps to ≈89.3–89.4%. The trade-offs are clear: ≈8.2% lower hydrogen consumption than Case 2, at the cost of ≈60% higher grid losses due to heavier flows.

IV. Conclusion

In this study, the objective was to maximize the restoration of both critical and non-critical loads during prolonged network outages while maintaining voltages within statutory limits. To achieve this, GreenShield Port was formulated as a mixed-integer quadratically constrained program on a modified IEEE-33 bus network, co-optimizing offshore wind-to-hydrogen conversion, a dual-mode hydrogen ferry, and a fleet of MFGs. The model scheduled 15-minute power dispatch, MFG routing/charging, and hydrogen flows under AC network and inventory constraints. Across three cases, all critical loads were restored, and a substantial share of non-critical demand was served. In the complete configuration (wind + ferry + storage), the ferry injected ≈18.1 MWh, the wind plant delivered ≈12.8 MWh to the grid and converted ≈5 MWh to hydrogen. The total served energy reached ≈89% over 24 h. Explicit tank management redefined the fleet as a peak-shaving reserve, reducing utilization to 39.2–57.5% and hydrogen consumption by ≈8.2% compared to the ferry-only case. However, it incurred higher line losses through internal transfers. Ultimately, all bus voltages remained within ±5% across all scenarios. These results confirmed that coordinated ship-to-grid, wind-to-hydrogen, and MFG deployment enhances service continuity and distribution-level resilience under disaster conditions.

References

[1] International Energy Agency (IEA), "Electricity security matters more than ever," in Power Systems in Transition. Paris, France: IEA, 2020.

[2] P. Gasser, et al., "A review on resilience assessment of energy systems," Sustainable and Resilient Infrastructure, vol. 6, no. 5, pp. 273–299, 2021.

[3] M. Maes, et al., "Data tool gives fine-grained view of climate vulnerabilities in the energy system and beyond," IEA Commentary, Nov. 2023

[4] X. Shan, X. Zhang, and C. K. Tse, "Identifying Sets of Critical Components That Affect the Resilience of Power Networks," IEEE Trans. Circuits Syst. II: Express Briefs, vol. 69, no. 12, pp. 4859–4863, Dec. 2022, doi: 10.1109/TCSII.2022.3188348.

[5] A. M. Asim, et al., "Integrated optimization of energy storage and green hydrogen systems for resilient and sustainable future power grids," Scientific Reports, vol. 15, Art. no. 25656, 2025.

[6] D. Kumar and A. Kumar, "Enhancing Microgrid Resilience Planning Through Optimized Demand Response". 2023, IEEE IICPE.

[7] Y. Men, et al., "Inverter-Dominated Networked Microgrids with Marine Energy Resources and Energy Storage Systems for Coastal Community Resiliency Enhancement, 2022" IEEE ECCE, pp. 3039–3045.

[8] Y. Zhang and P. Hu, "Optimal Exploitation of Mobile Emergency Generator and Distributed Energy Resource for Improving the Resilience of Incremental Power Distribution System under Extreme Grid Faults". 2021, IEEE ICEEMT, pp. 470–476.

[9] A. F. Malek, et al., "Resilience based decision metrics for dispatching mobile emergency truck generators in distribution system," in Proc. 2021 IEEE ICPEA, Shah Alam, Malaysia, Mar. 8–9, 2021, pp. 233–238.

[10] X. Zou, Y. Wang, and G. Strbac, "Resilience enhancement of multiple energy hubs via co-ordinated EV routing and scheduling, 2023" IEEE ISGT Europe, pp. 1–5, Oct. 2023.

[11] S. Zhu, et al., "Resilience-motivated service restoration of interdependent power and hydrogen distribution system," IEEE Access, vol. 12, pp. 149528–149542, Oct. 2024.

[12] Q. Li, et al., "Integrating Reinforcement Learning and Optimal Power Dispatch to Enhance Power Grid Resilience," IEEE Trans. Circuits Syst. II: Express Briefs, vol. 69, no. 3, pp. 1402–1406, Mar. 2022, doi: 10.1109/TCSII.2021.3131316.

[13] G. Liu et al., "EWELD: A large-scale industrial and commercial load dataset in extreme weather events," Scientific Data, vol. 10, art. no. 615, 2023.

979-8-3315-8138-1